Fuel 298 (2021) 120846

Contents lists available at ScienceDirect

Fuel

journal homepage: www.elsevier.com/locate/fuel

Full Length Article

Large eddy simulation on flame topologies and the blow-off characteristics of ammonia/air flame in a model gas turbine combustor

Xutao Wei [a], Meng Zhang [a,*], Zhenhua An [a], Jinhua Wang [a], Zuohua Huang [a], Houzhang Tan [b]

[a] State Key Laboratory of Multiphase Flow in Power Engineering, Xi'an Jiaotong University, Xi'an 710049, China
[b] MOE Key Laboratory of Thermo-Fluid Science and Engineering, Xi'an Jiaotong University, Xi'an 710049, China

ARTICLE INFO

Keywords:
Ammonia
Hydrogen carrier
Large eddy simulation
Thickened flame model
Blow-off

ABSTRACT

Ammonia (NH_3) is recently identified as one of the suitable energy carriers in hydrogen energy system. However, regarding NH_3 as a fuel is still facing several challenges which limit the direct use on modern combustion systems. The main challenge is the difficulty to stabilize NH_3/air flames. To reveal and analyze the stabilization mechanism and the characteristics during blow-off processes in a swirl combustor, large eddy simulation with thickened flame model was performed to resolve the three dimensional swirl NH_3/air flame. The CH_4/air flame was also performed for comparison. The reacting flow fields and the flame structures were measured by PIV and OH-PLIF technique respectively. For NH_3/air flame, flame fronts are burning to the higher equivalence ratio region, which leads to a larger trend of extinguishing. The curvature distribution at flame root is mainly dependent on the flame characteristics. Downstream the flows, the curvature distribution is mainly influenced by the flow field characteristics. Though the value of wall heat loss of NH_3/air flame is less than that of CH_4/air flame, the heat loss still shows greater influence on NH_3/air flame stabilization when considering the lower heat release rate of NH_3/air flame. The blow-off of CH_4/air flame is mainly caused by the decreasing HRR and heat loss, while for NH_3/air flame, it is a combined effect of the excessive stretch, the reduction of HRR as well as the greater heat loss effect.

1. Introduction

Ammonia (NH_3) is identified as one of the most promising energy carriers during the establishment of the future energy systems [1,2]. Ammonia is not only a carbon free fuel but also has 17.8% hydrogen by weight [3]. When comparing with hydrogen (H_2), NH_3 is much easier to liquefied (at the room temperature with about 8.5 bar, or at minus 33°centigrade and 1 bar) [4]. Moreover, due to the wide use of NH_3 as a chemical raw material, the carriage and storage technique have been well established [5,6]. Therefore, NH_3 used as the hydrogen carrier to store and transport energy is much more achievable and economical than the direct carriage and storage of compressed or liquid hydrogen (requiring 350–700 bar or −252.8℃) [4]. Downstream the energy system, NH_3 can also be converted back to H_2 by the procedure of dehydrogenation [3] or directly used as a fuel.

However, it is still challenging when using NH_3 as the fuel directly in modern gas turbines, internal combustion engines or other combustion systems. The challenges mainly include (a) the difficulties to stabilize NH_3 flames and the low thermal efficiencies resulted from lower heat release; (b) the unacceptable nitrogen oxide (NO_x) emissions due to the high nitrogen content in the molecule [3]. These challenges are attributed to the combustion properties and fuel molecule. Firstly the laminar flame speed of NH_3/air flame is very low, which is about one-fifth of methane/air (CH_4/air) flame at stoichiometric ratio conditions [7]. Moreover, the flame thickness is much thicker and the heat release rate (HRR) is much lower than that of CH_4/air flame. The adiabatic flame temperature is approximately 100–200 K lower than that of CH_4/air flames at the same equivalence ratio [3]. Though the flame is hardly to stabilize, recent experimental investigations showed that NH_3/air flames can be anchored in a swirl combustor [5,8], however within a limited stable range [9]. The lower combustion intensity nature, i.e., very small flame speed, leads to the larger probability to blow-off. Syred et al. [10] suggested that blow-off can be correlated with the inlet tangential velocity over a wide range of swirl numbers. The stable flame limits are hardly enhanced through solely increasing the swirl number [9]. On the other hand, researches show that there is great potential on stabilizing NH_3/air flames by blending with hydrogen or other hydrocarbon fuels, such as CH_4 or H_2 [11,12], diesel fuel [13], dimethyl ether

* Corresponding author.
E-mail address: mengz8851@xjtu.edu.cn (M. Zhang).

https://doi.org/10.1016/j.fuel.2021.120846
Received 10 February 2021; Received in revised form 6 April 2021; Accepted 8 April 2021

(DME) [14] and pulverized coal [3]. For example, adding small amount of CH_4 or H_2 can enhance the stable limits since the laminar flame speed is increasing and the combustion is getting more intensive [15,16]. In addition, direct combustion of liquid ammonia spray was achieved in a single stage swirl combustor recently [18]. Results show that there also exists some issues on flame stabilization in a gas turbines combustor of liquid ammonia spray [17]. The ammonia combustion is prone to local extinction and reignition during the equivalence ratio decreasing operation from a lean stable condition to blow-off. For ammonia swirl flame, the flame stabilization and blow-off process is largely depended on the structure of the flow, the flame properties. The investigation on the transient behavior of the blow-off process is vital to analyze the mechanisms of the process. However, few experimental studies are found in the literature on the blow-off issue of NH_3/air flame.

Numerical simulation is particularly significant, especially the large eddy simulation (LES) on combustion [9,18-20]. Somarathne et al. [21,22] employed three-dimensional LES by detailed chemistry and indicated that stable NH_3/air flames and NH_3/H_2 co-firing flames can be achieved using swirl combustors at different pressures. They analysis the flame stabilization by demonstrating the flow field and the combustion location. Honzawa et al. [23] employed a non-adiabatic flamelet generated manifold approach (NA-FGM) to simulate the NH_3/CH_4/air flames. Guo et al. [18,20] investigated the CH_4/air flame at near lean blow-off conditions [18], as well as CH_4/H_2/air flame at different blending ratios [20] on a swirl/bluff-body burner. The results suggest that more excessive strain rate and higher turbulence fluctuation can lead to the blow-off, and the increased heat loss by low temperature spot can enhance the flame attachment lift-off. Ma et al. [19] employed two numerical methods (a flamelet/progress variable model and a TF approach) and simulated stable conditions and a transient blow-out sequence of a swirl-stabilized CH_4/air flame. It was found that the variance of the integrated heat release is a sensible quantity as an early warning signal in detecting blow-out. In our previous investigation [9], LES with TF model was employed for both NH_3/air and CH_4/air flames on blow-off processes. The results showed that the NH_3/air flame has a faster blow-off process due to its the lower excessive stretch. In conclusion, the heat loss, heat release and excessive stretch are mainly considered during the analyses of the swirl flame instability, but the effect situations and degrees of these factors are still not clear on NH_3/air flames.

The objective of this study is to reveal and analyze the stability mechanisms on stable flames and the characteristics during blow-off process of an ammonia/air flame in a swirl stabilized combustor. Large eddy simulations with thickened flame model were performed to resolve the instantaneous three-dimensional evolution of the flame fronts and flow fields. The numerical results were firstly validated through he reacting flow fields and the flame structures, which were measured by Particle Imaging Velocimetry (PIV) system and Planar Laser Induced Fluorescence (PLIF) technique respectively. Then the detailed parameters of the flame fronts were demonstrated. The blow-off mechanism was investigated by analyzing the flame snapshots during the blow-off process. The paper is organized as following. The swirl burner and experimental measurements are introduced in Section2. Section3 describes the numerical models and methods. The results and discussions are shown in Section4. Section 5 concludes the paper.

2. Experimental description

2.1. Swirl Burner and flame conditions

Fig. 1 shows the premixed swirl burner schematically [9]. Fuel and air were fully premixed in the burner. Air (supported by a compressor) was introduced into the burner then accelerated and depressurized by a venturi geometry. At the throat of venturi, fuel was introduced by a multi-hole fuel injector and mixed with air downstream the throat. A perforated plate was employed just after the venturi to rectify the flow and further perturb the fuel/air mixture, as shown in Fig. 1(a). A swirler with 12 vanes and $\theta = 45°$ was mounted on a rod connected with the exit

Table 1
Parameters of the swirler.

Swirler	Type-45
D_i (mm)	18.0
D_o (mm)	35.0
θ (°)	45.0
Vanes	12
S	0.73

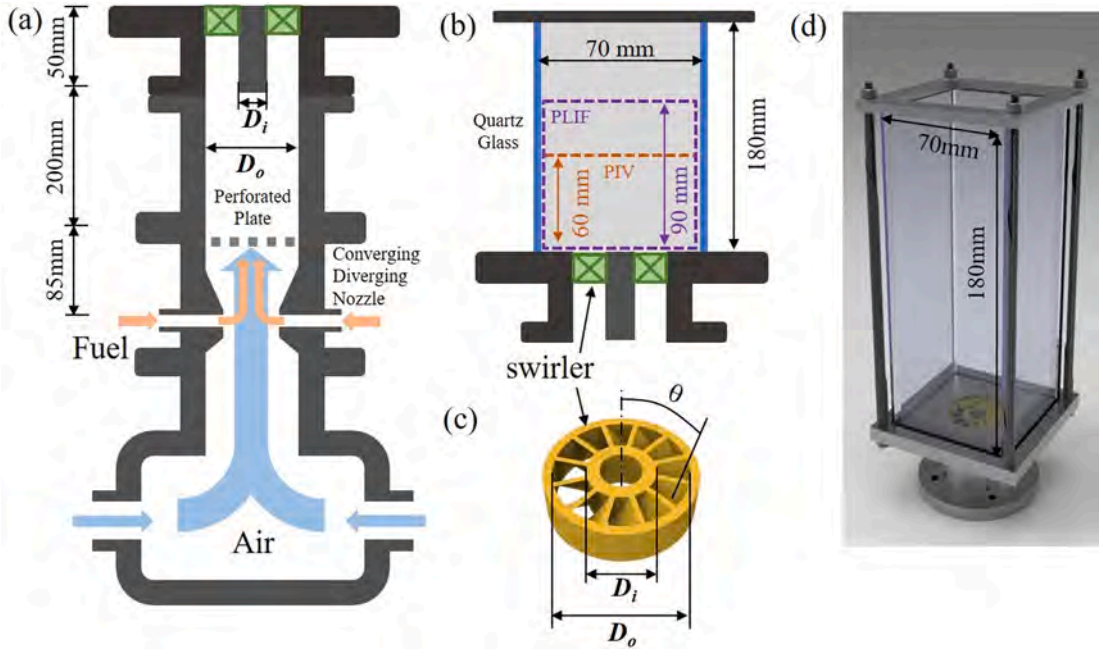

Fig. 1. (a) Schematic of the swirl burner; (b) the combustion chamber; (c) the swirler; (d) the 3D schematic of the combustor.

of the burner, shown in Fig. 1(a), (c). The parameters of the swirler are summarized in Table 1. The swirl number S is calculated by [24]:

$$S = \frac{2}{3}\frac{1-(D_i/D_o)}{1-(D_i/D_o)}\cdot tan\theta \quad (1)$$

A combustor liner placed downstream the burner exit with the quartz glass, with the dimension of 70 × 180 mm, at all sides to allow optical diagnostics, as shown in Fig. 1(d). The regions of the measurement windows for PIV (about 70 × 60 mm) and PLIF (about 70 × 90 mm) are enclosed by the dash lines in Fig. 1(b). The combustion performance of NH_3/air and CH_4/air flames was studied for various equivalent ratio in the previous studies [9,25]. According to the blow-off limits measured in Ref. [9], NH_3/air flame at $\phi = 0.7$ and CH_4/air flame at $\phi = 0.6$ with both bulk velocity U_b of 4 m/s were measured and simulated to further analyzing the flame topology and the blow-off characteristics. The operating conditions and the flame parameters are summarized in Table 2.

2.2. PIV and OH-PLIF measurement

PIV and OH-PLIF were conducted to measure reacting flow fields as well as flame structure [18,26]. The PIV system (LaVision Inc.) consists of a dual-cavity Nd:YAG laser (Litron) and a double shutter CCD camera (Imager LX 2 M). The Nd:YAG laser with 2 × 300 mJ pulse energy was operated at wavelength of 532 nm and repetition rate of 10 Hz. The CCD camera with a macro lens (100 mm, F/2.8) was placed at a measuring distance of 400 mm. The minimum time separation of the camera was 200 ns, and the visualized field was 1600 × 1200 pixels. A narrow bandpass filter (LaVision, 532 ± 5 nm, bandwidth of 10 nm) was mounted in front of the lens to collect the scattering signal. The instantaneous flame structure was measured by the OH-PLIF system (LaVision Inc.). The PLIF system has been introduced in detail in our previous studies [9,18,26], which is briefly introduced here. The system mainly includes a second harmonic pumped Nd:YAG laser, a pumped tunable dye laser as well as an ICCD camera. Firstly, the YAG laser (Quanta-Ray Pro-190) products the laser at pulse time of 10 ns with the wavelength of 532 nm with the laser energy of 300 mJ measured by a power meter (Edmund Optics, Model: Deluxe power meter). Secondly, the laser wavelength was adjusted to 566 nm and then to the OH excitation wavelength of 282.769 nm (with Coumarin 153 dye solution) in the dye laser (Sirah PRSC-G-3000). Then the laser passed through a sheet optics component to form a laser sheet with height of about 80 mm and thickness of about 0.5 mm at the center plane of flame. An ICCD camera (LaVision Image ProX) was located vertically with the laser sheet to detect OH fluorescence signal through a UV lens (Nikon Rayfact PF10545MF-UV), an OH bandpass filter (LaVision VZ08-0222) and an intensified Relay Optics (LaVision VC08-0094). The camera with the resolution of 1200 × 800 pixels was operated at exposure time of 2000 μs, gate width of 200 ns, delay of 100 ns and image sampling frequency of 10 Hz. The bulk flow rate of fuel and air was controlled precisely by the mass flow controllers (CS200, CS230A, SevenStar Co., Beijing China) with the uncertainty being ±1.5% of full scale.

Table 2
Summary of conditions. ϕ: equivalent ratio; U_b: the bulk velocity; Re: the Reynolds number; Q_{mass}: mass flow rate; *LHV*: lower heating value; *P*: the power output.

Conditions	ϕ	U_b (m/s)	Re	Q_{mass} (g/s)	*LHV* (MJ/kg)	*P* (kw)
NH_3/Air	0.70	4.00	1.28e4	0.249	18.6	4.63
CH_4/Air	0.60	4.00	1.28e4	0.0777	50.0	3.89

3. Numerical methods

3.1. Thickened flame model

Large eddy simulation (LES) combined with finite rate chemistry was conducted in present study. The scales lager than the grid size were resolved, while the smaller scales were modeled by a sub-grid scale tensor using eddy viscosity assumption. The dynamic Smagorinsky-Lilly model developed by Germano and Lilly was employed here for modeling the sub-grid viscosity [27,28]. The artificial thickened flame model developed by Colin et al. [29] was employed. The thickened flame front can be figured using a suitable thickening factor F (to keep at least 5–6 grids in the flame front [30]). The Navier–Stokes equations after spatially filtered can be found in Ref. [31]. The three-dimensional balance equation for instantaneous species mass fraction is shown as

$$\frac{\partial(\rho Y_k)}{\partial t} + \nabla(\rho \boldsymbol{U} Y_k) = -\nabla\cdot\left(F V_{k,i} Y_k\right) + \frac{\dot{\omega}_k}{F}, \quad k = 1, \cdots, N \quad (2)$$

where ρ is the density, U is and velocity vector, Y_k is species mass fraction of species k, $V_{k,i}$ is the diffusion velocity of species k, and $\dot{\omega}_k$ is the reaction source term. The unsteady conservation equation of instantaneous species mass fraction after a LES filter becomes

$$\frac{\partial\left(\bar{\rho}\widetilde{Y}_k\right)}{\partial t} + \nabla\left(\bar{\rho}\widetilde{\boldsymbol{U}}\widetilde{Y}_k\right) = -\nabla\cdot\left(F\Xi_\Delta\overline{V_{k,i}Y_k}\right) + \frac{\Xi_\Delta\overline{\dot{\omega}_k}}{F} \quad k = 1, \cdots, N \quad (3)$$

where Ξ_Δ is flame wrinkling factor which is used to offset the loss of the flame wrinkling after thickening. The filtered diffusion velocity was calculated by

$$\overline{V_{k,i}Y_k} = -\bar{\rho}D_k\nabla\widetilde{Y}_k \quad (4)$$

where D_k is the mixture-averaged molecular diffusion coefficient of species k and calculated by

$$D_k = \frac{1-x_k}{\sum_{j\neq k}^{N}\left(x_j/D_{jk}\right)}, \quad k = 1, \cdots, N \quad (5)$$

where x_k is the mole fraction of species k, D_{jk} is the binary diffusion coefficient of species j and k. A flame wrinkling factor Ξ_Δ given by [30,32]

$$\Xi_\Delta = \left\{1 + min\left[max\left(\frac{\Delta}{\delta_l} - 1, 0\right), \Gamma\left(\frac{\Delta}{\delta_l}, \frac{u'_\Delta}{S_l}, Re_\Delta\right)\frac{u'_\Delta}{S_l}\right]\right\}^\beta \quad (6)$$

where Δis the filter width, u'_Δ is the subgrid turbulence intensity, Re_Δ is the subgrid Reynolds number, and β is the model coefficient. In present simulation, $\beta = 0.5$ is performed for the purpose of reducing the amount of calculation [18,33]. For thickening both reacting zone and preheated zone effectively, a well-proved dynamically thickened flame model is employed [33]. The thickening factor is calculated by:

$$F = 1 + (F_0 - 1)tanh(\alpha\cdot\Omega) \quad (7)$$

where F_0 is the maximum thickening factor, α is a constant to control the thickness between $F = F_0$ (thickened) and $F = 1$ (non-thickened). The probe function Ω is defined as $16c(1\text{-}c)^2$ [34]. The progress variable c was calculated by the mass fraction Y_{NH3} or Y_{CH4} ($c = 0$ in unburnt premix gas and $c = 1$ after flame).

3.2. Chemical reaction mechanism

Through the chemical kinetic mechanisms of ammonia have been extensively studied [35,36], these earlier developed mechanisms have tremendous number of species and reactions, which can be hardly applied in three-dimensional LES of a real swirl burner. The mechanism reported by Miller [37] was applied in some researches [21,22] because

of its fewer species and reactions, although the laminar flame speed S_L and ignition delay time of Miller's mechanism cannot be predicted very well. More recently, the kinetic models of ammonia reported by Stagni et al. [38], Mathieu et al. [39], and Otomo et al. [40] with about 35 species and 220 reactions have been well verified and can be easier employed in the calculations [41]. Here, we intend to compare NH_3/air flame and CH_4/air flame. Therefore, the kinetic model should be kept the same in both conditions to eliminate the uncertainties from chemical reaction mechanism. Xiao et al. [42] newly conducted a study on NH_3/CH_4/air reduced mechanisms from Konnov's mechanism [36]. Five reduced mechanisms of NH_3/CH_4/air co-firing flame were validated not only by the laminar flame speed, ignition delay time but also the turbulent combustion in more practical conditions. A reduced mechanism with 31 species as well as 243 reactions from Xiao et al. was employed in the current study. The one-dimensional, adiabatic, unstretched laminar flames were calculated using the PREMIX code in the ANSYS Chemkin-PRO package [43]. Thermal diffusion and multi-component transport were included in the 1D simulation. The laminar flame thickness is defined by $\delta_L = \frac{T_{ad}-T_0}{max(\mathrm{d}T/\mathrm{d}x)}$. T_{ad} is the adiabatic flame temperature, T_0 is the initial temperature, and max(dT/dx) is the maximum of the slope of temperature curve.

3.3. Computational domain and simulation details

The numerical domain as shown in Fig. 2(a) consists of a square combustor (70 mm × 70 mm × 180 mm) and an upstream swirler with inlet pipe (about 35 mm × 20 mm × 2π), which is exactly with the same size in the experiments. The inlet pipe walls, swirler and the bottom of combustion chamber were set as an adiabatic and non-slip condition, while the isothermal boundary was specified for the four walls around (quartz glass liner in experiments). In the current study, the isothermal wall was T_{wall} = 450 K for NH_3/air flame while T_{wall} = 750 K for CH_4/air flame according to the measurement in experiments. The overall mesh and local grid information are shown in Fig. 2(b) and (c). The whole computational domain is divided into 274 blocks and contains about 5 million non-uniformed structured grids. At the flame region, the size of girds was about 0.5 mm. The grid independence was verified by further refining the mesh to 7 million, and the results showed no effect on the statistics of the flow field. The adiabatic flame temperature and major TF model characteristic parameters are summarized in Table 3. The thickening factor F is of 3 for both conditions to prevent from covering up the thickness distinction. The simulation is implemented in OpenFOAM. The gradient and laplacian terms were discretized by a second-order accuracy TVD schemes. The transient term was discretized by implicit Euler scheme. The residuals criterion of velocity, pressure, enthalpy and species mass fraction were 10^{-7}, 10^{-6}, $10^{-7}$and 10^{-6} respectively. The maximum Courant number during the simulation was always<0.3, and the time step was set as $\Delta t = 1e^{-6}$ for both conditions.

Table 3
Summary of characteristic parameters. T_{ad}: Adiabatic flame temperature; Δ: grid size in the main reaction zone; n: number of grid number inside the flame front.

Conditions	ϕ	T_{ad} (K)	Δ (mm)	Δ/δ_L	n	F
NH_3/Air	0.70	1704.44	0.50	0.33	5	3
CH_4/Air	0.60	1667.74	0.50	0.41	5	3

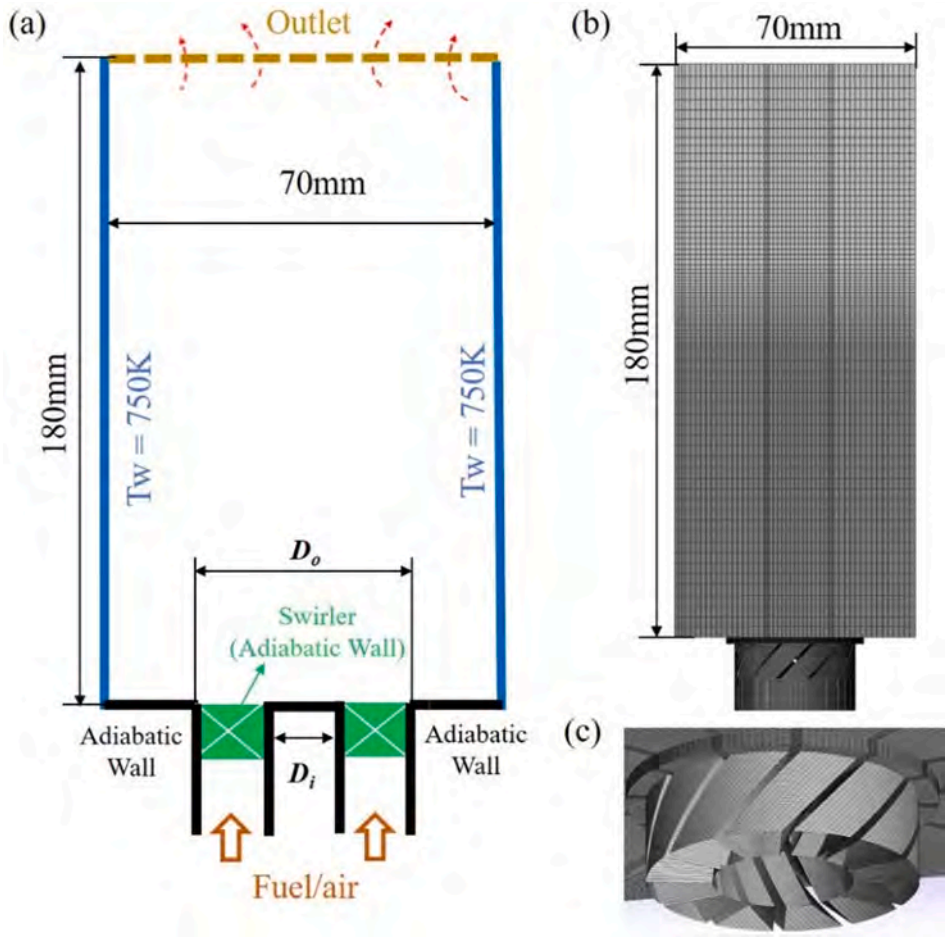

Fig. 2. (a) Computational domain; (b) global grid information; (c) local grids of the swirler.

4. Results and discussions

4.1. Model validation

The experimental and LES results of mean reacting flow velocity are included in Fig. 3. The comparison shows the numerical method can well predict the reacting flow velocity fields. The flow downstream the burner exit forms a large toroidal vortex-type recirculation zone due to the swirler structure, i.e., inner recirculation zone (IRZ). The central range of IRZ shows negative of velocity which facilitates the mixing of radical species, hot combustion products and the incoming reactants [44]. The glass liner confines the flow and collides with the flow at the location of about 30 mm in height, which forms the outer recirculation zone at the corner (ORZ). Two regions with a large gradient of velocity are defined as locations of the inner shear layer (ISL) and outer shear layer (OSL). For further quantitative comparison, mean axial and azimuthal velocities for CH_4/air and NH_3/air flames are presented in Fig. 4. It can be seen that two recirculation zones and two shear layers have been well predicted by LES. The difference near the bottom of combustion chamber (y = 10 mm) mainly comes from the adiabatic boundaries of the swirler and burner exit. The data near the glass liner (x=±30-35) also represents some discrepancies. The reason is construed as isothermal boundary was employed on walls around.

The flame structures obtained from LES and measured by OH-PLIF are compared in Fig. 5. The OH-PLIF measurements were employed at same laser energy, OH radical excitation wavelength, and post-processing procedure. It is clear that the intensity of OH signal on CH_4/air flame is much stronger than that on NH_3/air flame (as shown in Fig. 5 (a) and (c)). This illustrates that there are less OH radical in NH_3 flame which can raise measuring problems of obtaining NH_3/air flame structure, especially at the conditions near lean blow off [9]. Mass fraction of OH radical on LES is shown in Fig. 5(b) and (d). The current LES method can generally predict the flame macrostructure of both flames. However, the flame front in ORZ or OSL for CH_4/air flame has not been perfectly captured, which mainly resulted from the difference between the actual temperature distribution and isothermal approximation on side walls. Considering that the reactions proceed in or close to ISL and the reaction zone is thickened artificially, the differences are acceptable. For "V" shape flame (defined in Ref. [9]), the flame mainly stabilized in the low velocity zone of the inner shear layer. In all, good agreement with the experiment results is achieved by the LES method with thickened flame model.

4.2. Flame characteristics near blow-off conditions

For revealing the different stabilization features of NH_3/air flame, several characteristical parameters are compared with CH_4/air flame in this section. Firstly, the local equivalence ratios were calculated by the mixture fraction equations to analyze local distinctions. Although the fuel and air have already premixed, local equivalence ratio varies and represents the local change of fuel and O_2 quantitatively [45]. The mixture fraction equations based on Bilger's mixture fraction formulation [46] are shown as:

$$z_{NH3} = \frac{0.25(z_H - z_{H,2})/w_H + 0.75(z_N - z_{N,2})/w_N - (z_O - z_{O,2})/w_O}{0.25(z_{H,1} - z_{H,2})/w_H + 0.75(z_{N,1} - z_{N,2})/w_N - (z_{O,1} - z_{O,2})/w_O} \tag{8}$$

$$z_{CH4} = \frac{0.5(z_H - z_{H,2})/w_H + 2(z_C - z_{C,2})/w_C - (z_O - z_{O,2})/w_O}{0.5(z_{H,1} - z_{H,2})/w_H + 2(z_{C,1} - z_{C,2})/w_C - (z_{O,1} - z_{O,2})/w_O} \tag{9}$$

where z_H, z_N, z_O, and z_C represent the local elemental mass fractions of hydrogen, nitrogen, carbon, and oxygen respectively. w_H, w_N, w_O, and w_C represent the relative atomic mass. The subscripts 1 and 2 correspond to the mixture and ideal composition air (0.23 of O_2 and 0.77 of N_2) respectively. Then the local equivalence ratio of NH_3 and CH_4 can be defined as[45]:

$$\phi_{local} = \frac{z(1 - z_{St})}{z_{St}(1 - z)} \tag{10}$$

where z_{St} represents the mixture fraction at the stoichiometric equivalence ratio condition, i.e., 0.142 and 0.055 for NH_3/air and CH_4/air flames respectively. Once ϕ_{local} is defined, the angle between the directions of the ϕ_{local} and the temperature gradient can be calculated by [47]:

$$cos(\alpha) = \frac{\nabla\phi_{local}\cdot\nabla T}{|\nabla\phi_{local}|\cdot|\nabla T|} \tag{11}$$

The normal vector of the ϕ_{local} is employed as from rich ϕ_{local} to lean. The positive normal vector of the temperature is defined as from low temperature (unburnt) to high temperature (burnt). Using the definition of cos(α), we can make a judgment whether the flame is propagating to the lower or high ϕ_{local} region. When cos(α) is at [0,1] as the angle is smaller than 90°, the flame is on a tendency of propagating to the lower ϕ_{local} region. Pires et al. [48] suggested that when the flame is burning to the lower equivalence ratio region, the flame propagation velocity increases and the stabilization limits are widened. The curvature κ can be obtained from the normal vector of the temperature, calculated by [18]:

$$\kappa = -\nabla\cdot(\nabla T/|\nabla T|) \tag{12}$$

The flame front convex/concave to the unburnt gas is defined as positive/negative curvature, respectively.

Fig. 6 shows the cos(α) and κ on an instantaneous flame front. To clearly compare the two cases, the absolute value of κ is present here. It is evident that both cases are at stable flame conditions. For CH_4/air flame, cos(α) is largely distributed at [0, 1], and nearly no flame front with negative cos(α) is observed. In comparison, more flame front with negative cos(α) is seen for NH_3/air flame. The flame front wrinkles can be divided into two parts as convex to the unburnt mixture (positive curvature part) and concave to the unburnt mixture (negative curvature part). In this study, we mention the positive curvature as "ridges" and the negative curvature to "valleys", as shown in Fig. 6(d). The number of the ridges and valleys is same for both flames because of the same swirler vanes number of 12. The flame front is restricted by the side walls downstream the flow at about y = 30 mm which is defined as the collision location of flames. The flame front characteristics show significant differences downstream the collision location, as shown in Fig. 6, in which the side walls make a contribution to reducing the differences of curvature. When comparing Fig. 6 (c) (d), it can be seen that less large $|\kappa|$ areas are found near the burner exit in the NH_3/air flame front, which happens in both ridges and valleys. This illustrates that NH_3/air flame front near the burner exit has more large scale wrinkles and less small scale wrinkles. The curvature differences between two

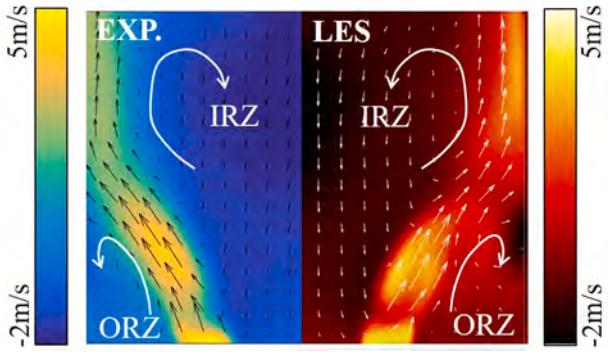

Fig. 3. Mean reacting flow velocity field of NH_3/air flame. Left: the PIV measurement result; right: the LES result. (ORZ is the outer recirculation zone; IRZ is the inner recirculation zone).

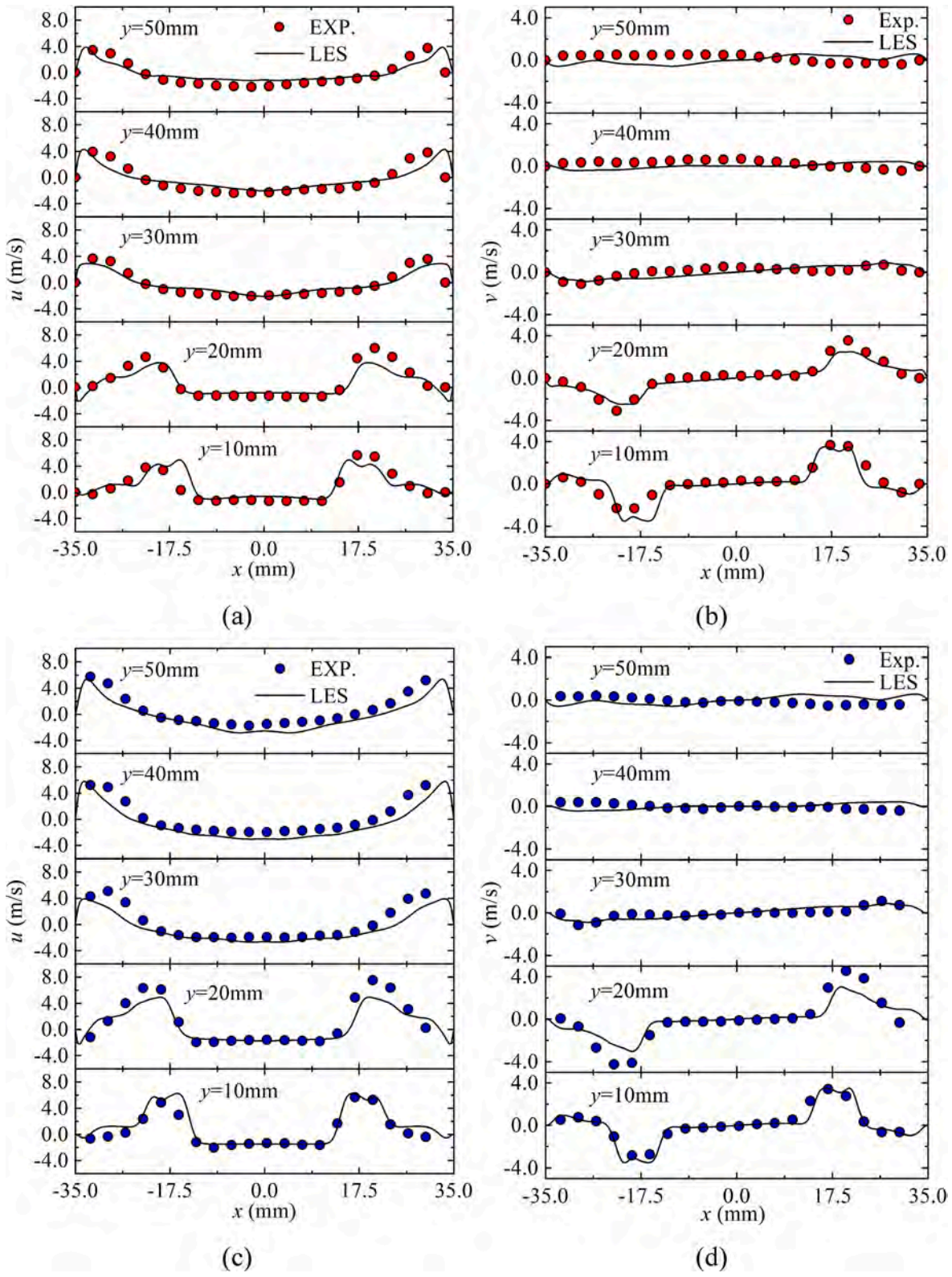

Fig. 4. Comparisons of mean axial velocity (left) and mean azimuthal velocity (right) of the reacting flow field of NH_3/air flame (top) and CH_4/air flame (down) between PIV results () and LES () at different axial positions: $y = 10, 20, 30, 40, 50$ mm.

conditions downstream the collision location are hard to be found with Fig. 6. Hence, the quantitative analyses of $\cos(\alpha)$ and κ are provided below.

The statistics of OH mass fraction Y_{OH} and progress variable c colored with $\cos(\alpha)$ in different height are shown in Fig. 7. The data is taken from the horizontal plane of $y = 20$ mm as upstream location before collision, and $y = 30$ mm as the location of collision. The black dotted line represents the variation of 1D laminar flame. The logarithmic coordinate is employed here to clear the variation of Y_{OH} and c. At $y = 20$ mm, shown as Fig. 7(a) (c), both flames have a large portion of the flame front at cos

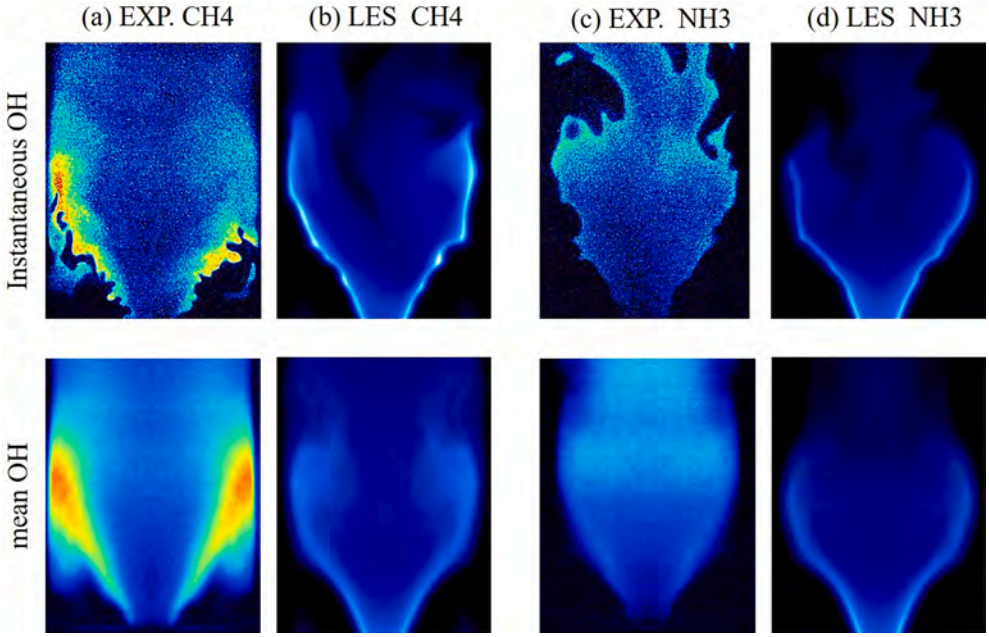

Fig. 5. The comparison of flame structure of NH_3/air flame and CH_4/air flame. Up: instantaneous OH; down: mean OH.

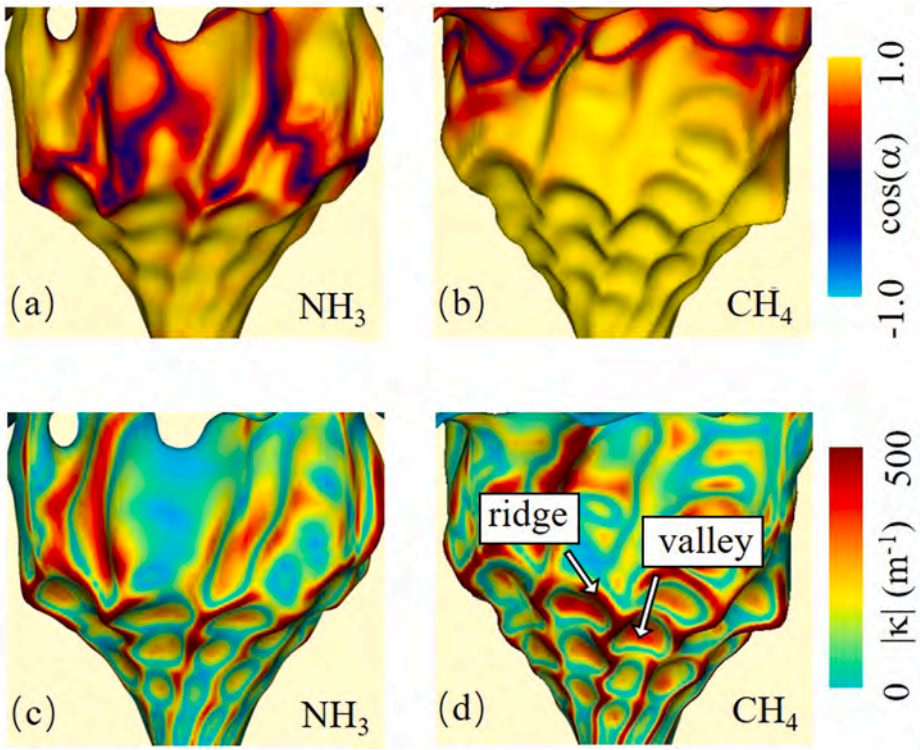

Fig. 6. The flame front with cos(α) (top) and absolute value of curvature (bottom). Left: NH_3/air flame; right: CH_4/air flame. The structures of ridges and valleys are indicated in (d).

(α)≈1 which distributes near the 1D laminar flame results. However, it is clearly seen that for NH_3/air flame, there are negative values of cos(α) scattered from the 1D result. And these negative cos(α) is mainly comes from $c < 0.5$. For CH_4/air flame within $0.3 < c < 0.6$, cos(α) of the scattered distribution is still mostly near 1.0 and few negative cos(α) is obtained. When comparing two flames, it is clear that more negative cos (α) are found on NH_3/air flame. This indicates that although the equivalence ratio is set at stable flame conditions, there are still more locations in the NH_3/air flame burning to the higher equivalence ratio region. This feature leads to a narrower stabilization limits and a larger trend of extinguishing according to Ref. [48]. Downstream the chamber, when comparing in Fig. 7 (b) (d), negative cos(α) of NH_3/air flame are still more than that of CH_4/air flame. Moreover, the negative cos(α) can also be found at $0.5 < c < 1.0$ in NH_3/air flame. This indicates that when downstream the chamber, the tendency of extinguishing in NH_3/air flame case increases, while it in CH_4/air flame case is essentially unchanged.

Fig. 8 shows the curvature probability density function distributions

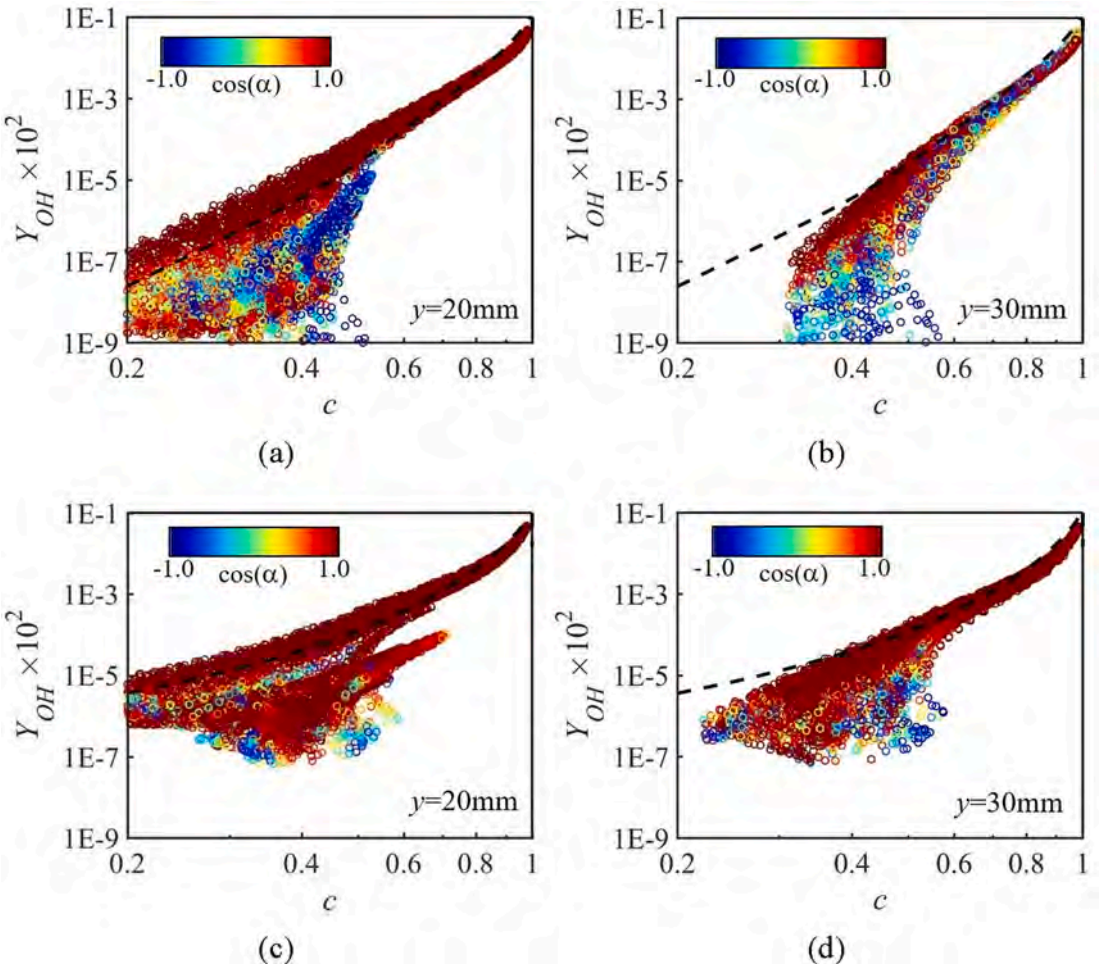

Fig. 7. cos(α) of the flame front at different height of y = 20 mm and y = 30 mm. Top: NH_3/air flame; bottom: CH_4/air flame. The black dotted line represents the results of 1D laminar simulation.

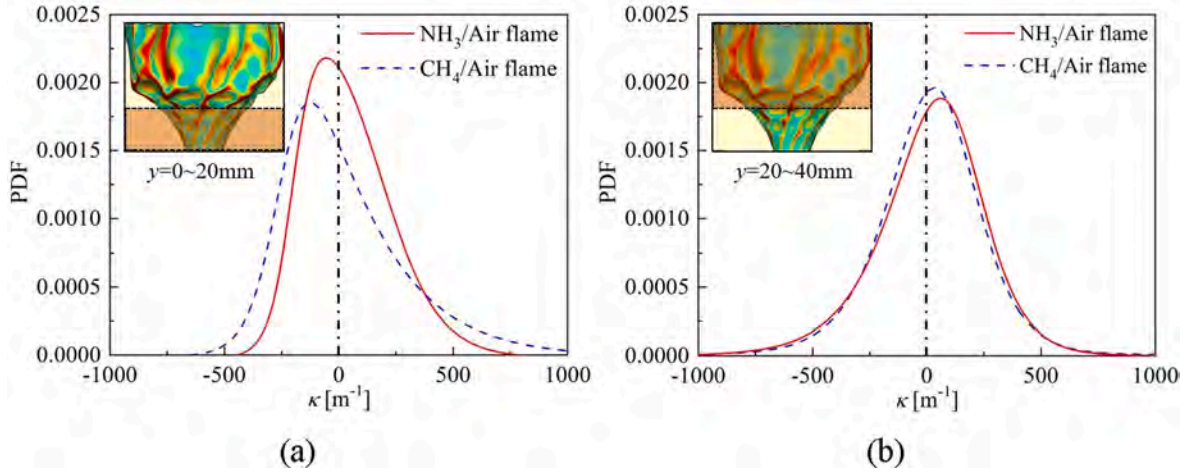

Fig. 8. Curvature probability density function distributions on different height ranges of NH_3/air and CH_4/air flame. (a): y = 0–20 mm; (b): y = 20–40 mm.

on different height ranges of NH_3/air and CH_4/air flames. The curvature was obtained with the flame front of c = 0.9. Fig. 8(a) shows the curvature statistics at $0 < y < 20$ mm, as the range from flame root to the flame collision location. Fig. 8(b) represents curvature statistics at y = 20–40 mm covering the location after the flame collision. Comparing the curvature PDF of two flames at y = 0–20 mm, the peak of curvature PDF distribution of NH_3/air flame is higher and the PDF profile is narrower comparing with CH_4/air flame. This further illustrates that there are more large-scale flame and less small-scale wrinkles for NH_3/air flame, which is also observed in the OH-PLIF 2D results in Fig. 5. This is due to the fact that turbulence-flame interaction is less active to form large-scale wrinkle structures because of the larger flame thickness. Furthermore, the curvature corresponding to the peak PDF values for both flames is negative value. This illustrates that the valley structures in

flame front are more frequent than that of the ridge structures. Downstream the chamber, the curvature at $y = 20$–40 mm is also counted in Fig. 8(b), showing same distributions for both flames. The curvature at $y = 20$–40 mm at peak locations of PDF of both flames is at a small positive value, indicating the convex structure to unburned mixture are more frequent. The distributions in Fig. 8(b) are resulted from the impact of the turbulent boundary layer, which is resulted from by the liner walls. The turbulent boundary layer smoothens the flame front and makes a contribution to reducing the differences of curvature. On the other hand, the similar large recirculation zone leads to the flame front turning inward at the downstream locations ($y > 30$ mm). The analysis indicates that for swirl flames in present study, the curvature at flame root is mainly decided by the flame characteristics (fuel or ϕ). Downstream the flame, however, the curvature probability density function distributions are mainly influenced by the flow field characteristics.

When the flame is close to the blow-off limits, the local vortex stretch is regarded as a crucial influence factor to extinguish the flames [9,18]. The total stretch suffered by the flames is defined consisting of the effects of the strain and curvature, given by:

$$\mathrm{K} = S_L\kappa + K_s \tag{13}$$

where κ is the curvature, and K_s is the strain rate defined as $K_s = -\boldsymbol{n}\cdot\boldsymbol{E}\cdot\boldsymbol{n}$. E is the rate of strain tensor, written as $\boldsymbol{E} = \frac{1}{2}[\nabla\boldsymbol{u} + \nabla\boldsymbol{u}^{\mathrm{T}}]$. $\boldsymbol{n} = \frac{\nabla T}{|\nabla T|}$ is the unit normal vector of the flame front, which is the same *iso*-surface as used in κ definition. u represents the flow velocity at the flame location. The extinction stretch (K_e) is calculated by opposed-flow flame model using CHEMKIN PRO [43] with the same chemical reaction mechanism mentioned in Section 3.2. K_e is of about 40 s^{-1} and 500 s^{-1} for NH_3/air and CH_4/air flames, respectively. The excessive stretch is defined as the difference between the total stretch K and the extinction stretch K_e, given by:

$$K_{excessive} = \mathrm{K} - K_e \tag{14}$$

Fig. 9 shows the joint PDF distributions of the stretch and the curvature. The extinction stretch K_e is also marked by red dashed lines in the figure, while the black lines donate the conditioned averaged value. CH_4/air flame burns at a lager range of stretch value of about $\mathrm{K_{max}} = 2000\ s^{-1}$ which is about twice comparing with that of NH_3/air flame. For CH_4/air flame, a large portion of the flame front area is under the extinction stretch K_e, see Fig. 9 (b). The statistics show that these flame front with excessive stretch is mainly distributed near the zero value of curvature. However, due to the significant lower K_e of the NH_3/air flame, there are more flame front area suffering the excessive stretch, as shown in Fig. 9 (a). The significantly different excessive stretch feature between these two flames is one of the reasons leading to distinct stabilization characters and blow-off limits. Moreover, the maximum stretch value positions for both flames correspond to the negative curvature, which indicates that the flame front at $y < 20$ mm play a major role on curvature distribution.

Chamber wall heat loss is another pronounced reason effecting flame speed for ammonia/air flame when comparing with CH_4/air flame [23]. In the other words, NH_3/air flame is more susceptible by the chamber wall heat loss when stabilizing the flames in a swirler. The effect of convection heat loss rate is analyzed for both flames in Fig. 10. The convection heat flux between the combustor walls and the burnt gas is calculated by

$$q = \frac{\lambda \mathrm{Nu}_m}{l}\left(T_g - T_w\right) \tag{15}$$

where λ is the thermal conductivity, l is the length of the walls, and Nu_m is the mean Nusselt number calculated by an experiential formula [49]. T_g and T_w is the temperature of the gas and the combustor walls respectively. Fig. 10 shows the variation of the mean temperature, heat release rate (HRR), convection heat loss (CHL) and the ratio of HRR/CHL along the height (y direction). The mean temperature of CH_4/air flames is higher than that of NH_3/air flame. The lower heat release rate of NH_3/air flame can be seen in Fig. 10 (b). Fig. 10 (c) presents the rate of convection heat loss calculated using the mean temperature in Fig. 10 (a) and the temperature of the isothermal boundary. It shows that the convection heat loss rate of CH_4/air flame is much higher than that of NH_3/air flame because of the higher gas temperature. However, when dividing the mean HRR into CHL, as shown in Fig. 10 (d), the differences between two flames is very small. Particularly within $y = 0$–45 mm, the CHL/HRR of NH_3/air flame is larger, illustrating that the chamber wall heat loss shows greater influence on flame stabilization, although the absolute value of convection heat loss rate of ammonia fuel is less than methane.

4.3. Blow-off characteristics

To investigate the flame dynamics during the blow-off process, the equivalence ratio in the simulations is impulsively decreased to a nonflammable equivalence ratio of $\phi = 0.3$. Mixture inlet velocity is fixed while the mass fraction of fuel, O_2 and N_2 at the inlet boundary is suddenly varied. The temporal evolutions of volume-averaged

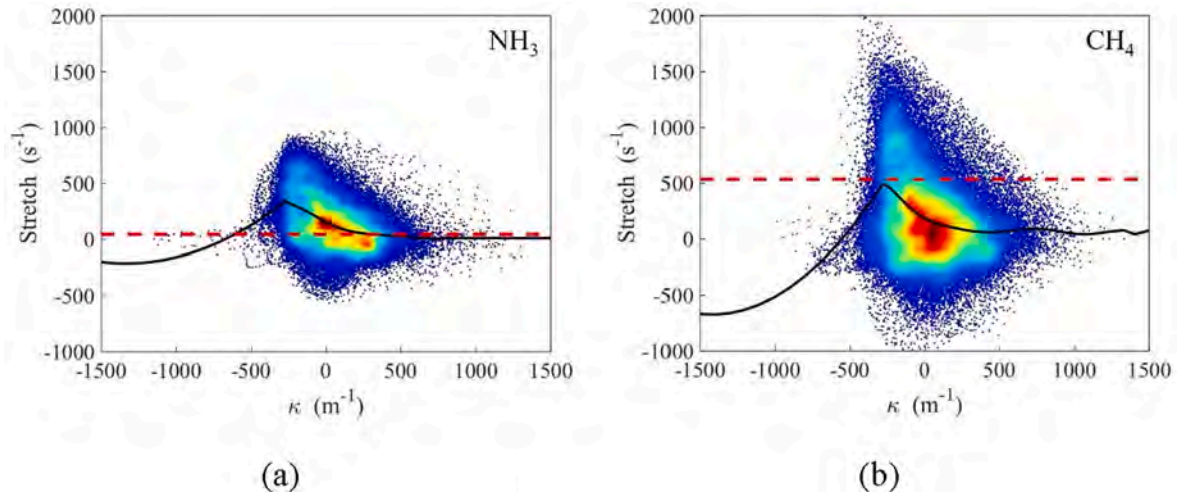

Fig. 9. The joint PDF distributions of stretch and curvature obtained from entire flame front which is defined by $c = 0.9$. (a) NH_3/air flame; (b) CH_4/air flame. The red dashed line and black line donate extinction stretch K_e and the conditional average of stretch, respectively. (For interpretation of the references to colour in this figure legend, the reader is referred to the web version of this article.)

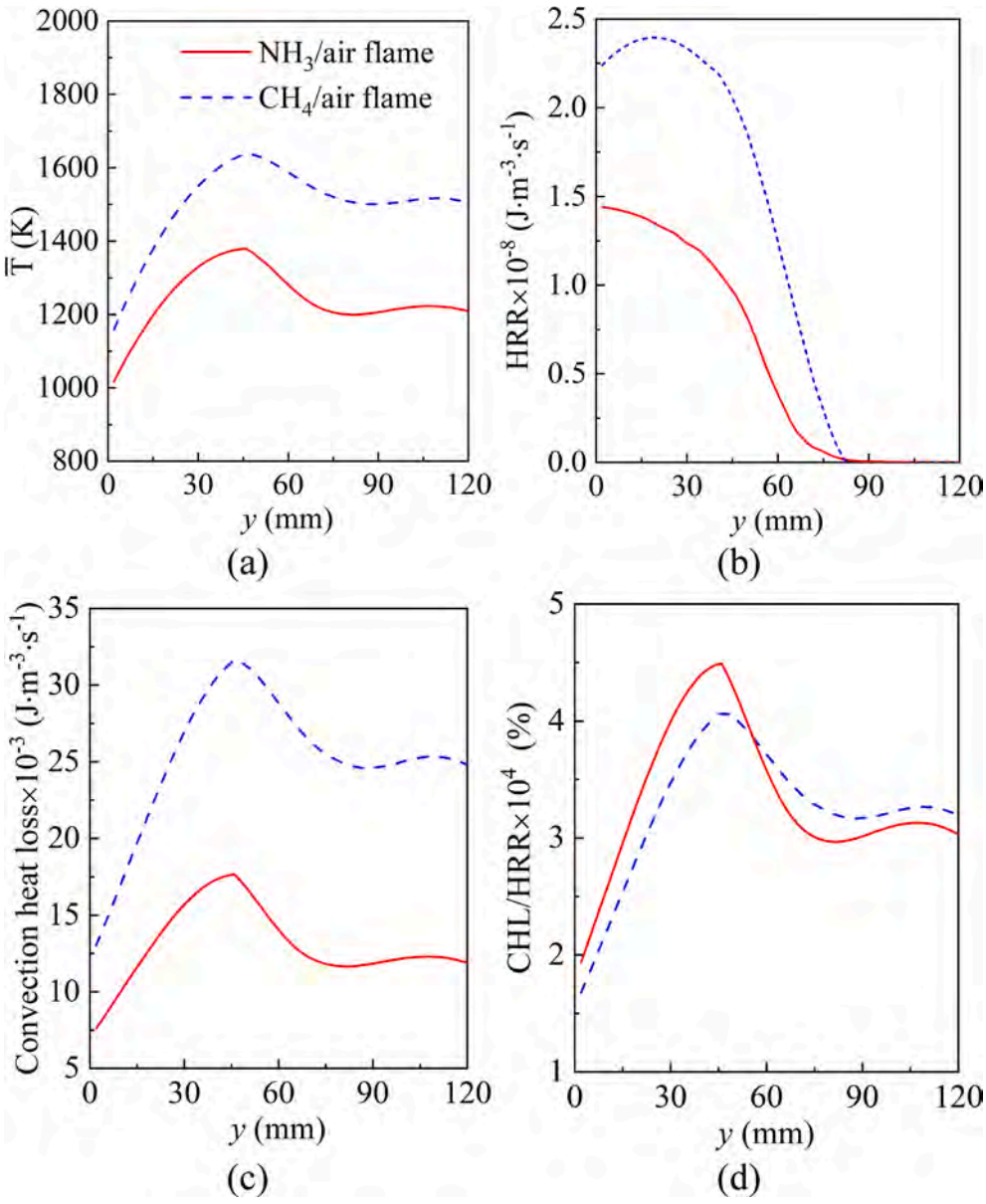

Fig. 10. Parameters variation of the average in the horizontal direction (x direction) along the height direction (y direction). (a) Average temperature; (b) heat release rate HRR; (c) the rate of convection heat loss CHL; (d) ratio of CHL to HRR.

temperature, OH mass fraction, HRR and ratio of CHL to HRR from $t = 0$ ms to 20 ms are shown in Fig. 11. 0 ms corresponds to the instance of the change in equivalence ratio. The temperature of both fuels presents similar gradually decreasing feature, while the temperature of CH_4/air flame is always larger than that of NH_3/air flame, shown in Fig. 11(a). The resistance of the heat release after the change in inflow conditions can be clearly observed in NH_3/air flames. Three different phases for the blow-off sequence can be defined. In order to comparing two flames, the different phases are also shown for CH_4/air flame. The change between the phases of CH_4/air flame is a bit hysteretic comparing to the NH_3/air flame. At the first phase, OH mass fraction of NH_3/air flame decreases faster than that of CH_4/air flame, while HRR of both flames decreases sharply due to the less fuels. The CHL/HRR increases in the first phase to the same value. At the second phase, the HRR and OH mass fraction of NH_3/air flame increase, which is defined as a resistance phenomenon. For CH_4/air flame, a faint resistance is found that the slope of HRR rapidly diminishes, but HRR still decreases by a gentle slope. The effect of CHL in NH_3/air flame decreases rapidly due to the rise of HRR. Ma et al. [19] suggested that the resistance of HRR can extend the total blow-off time. Nevertheless, as shown in the third phase where HRR and OH mass fraction decrease evidently, the blow-off process of NH_3/air flame is still faster than that of CH_4/air flame, although the more significant resistance phenomenon is observed. When comparing values of CHL/HRR in the third phase, it grows much faster for NH_3/air flame. In summary, the reason of faster blow-off process of NH_3/air flame is mainly attributed to the much lower HRR of stable condition as well as the more remarkable effect of the heat loss during blow-off.

The time evolution of HRR field, OH mass fraction field and the excessive stretch field, as well as the joint PDF between stretch rate and chemical reaction rate are shown in Fig. 12. K_e is marked by red dotted lines in the figure. The blow-off is defined as the time when the instantaneous HRR decreased down to 50% of its maximum value, which is about 16 ms and 20 ms for NH_3/air and CH_4/air flames, respectively. Researches [13,14] show that NH_3/air flame presents longer ignition delays and lower flame speed due to its high auto ignition temperature and low chemical reactivity, which leads to a larger tendency to blow off. The differences can be easily observed when comparing two blow-off processes. For NH_3/air flame as shown in

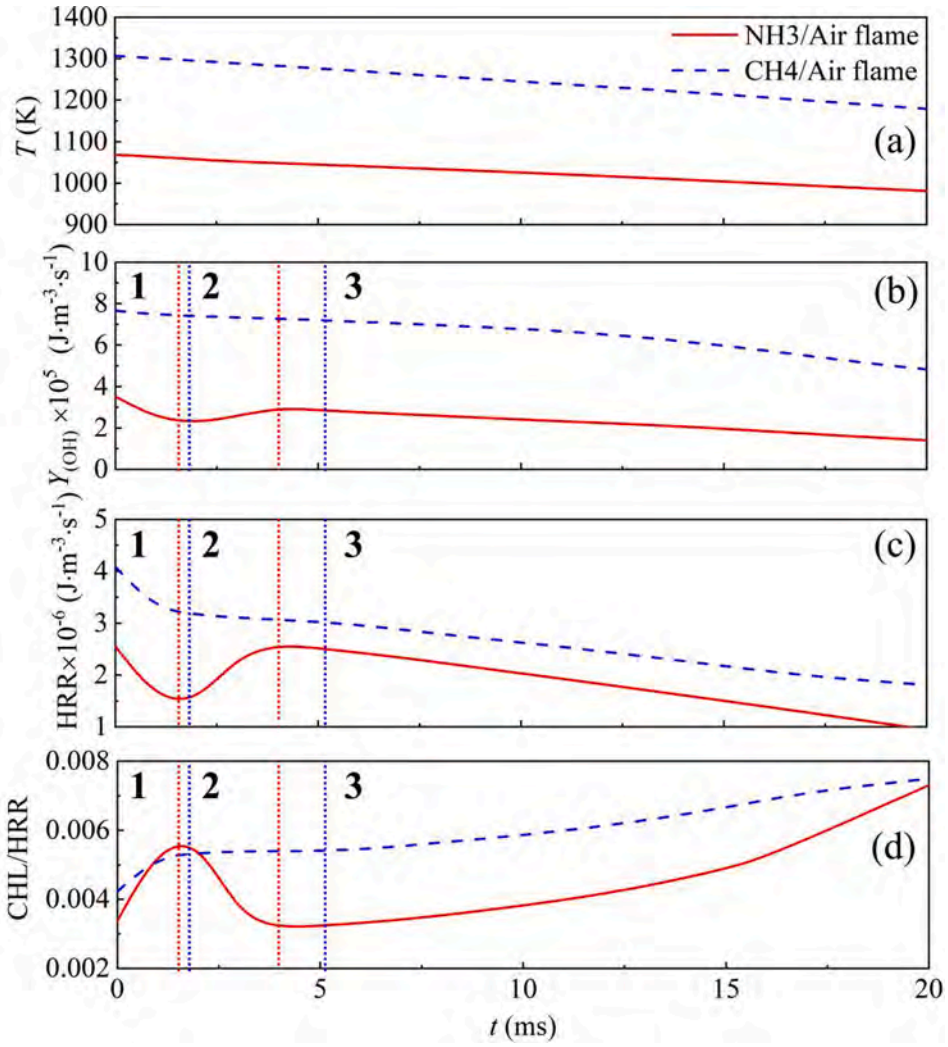

Fig. 11. Temporal evolution of (a) volume-averaged temperature, (b) OH mass fraction, (c) heat release rate, and (d) ratio of CHL to HRR. Three phases for the blow-off sequence are defined.

Fig. 12(a), more than 50% percentage of flame front area is at the stretch lager than K_e (the excessive stretch condition), even during the blow-off process. This illustrates the excessive stretch still plays an important role when NH_3/air flame blows off. The root of the flame extinguishes firstly due to the change of the upstream equivalence ratio, and the extinction region develops downstream leading to the flame blow-off. The resistance feature can also be observed at 4 ms of NH_3/air flame since several locations of flame is still on high HRR value shown in the instantaneous HRR distribution. In comparison, only a small part of flame front is at the excessive stretch condition in CH_4/air flame during blow-off process. The chemical reaction rate of fuel consumption decreases with the reduction of HRR for both conditions. The blow-off processes indicate that the two major factors, the excessive stretch on the flame front and the reduction of global HRR, show different impact on blow-off characteristics of different fuels. For CH_4/air flame, the blow-off is mainly caused by the decreasing HRR, while for NH_3/air it is the combined effect of the excessive stretch as well as the reduction of HRR causing blow-off. The comparison of evolution process of the instantaneous excessive stretch illustrates that the excessive stretch affects different height ranges of the two flames. The excessive stretch effects for CH_4/air flame are mainly observed at flame root before the collision location ($y < 30$ mm) for CH_4/air flame, while the entire flame front is at the excessive stretch conditions for NH_3/air flame.

5. Conclusions

In this study, large-eddy simulations with thickened flame model were performed to resolve the instantaneous three-dimensional NH_3/air and CH_4/air flames in a swirl combustor. The reacting flow fields and the flame structures measured by PIV and OH-PLIF techniques show that the LES can well predict both flames. The stable conditions and blow-off evolutions of both flames were compared to reveal the mechanism of the blow-off characteristics. Main conclusions are summarized as follows:

1. NH_3/air flame has more flame area tending to burning to high equivalence ratio region, which leads to a narrower stabilization limits and a larger trend of extinguishing. The tendency of extinguishing of NH_3/air flame increases downstream, while this feature of CH_4/air flame is essentially unchanged.
2. For swirl flames, the curvature at flame root is mainly dependent on the flame characteristics. Downstream the flame, the curvature probability density function distributions are mainly influenced by the flow field characteristics. There are more large-scale flame wrinkles for NH_3/air flame. The turbulence-flame interaction is less active to form small-scale wrinkle structures due to the larger flame thickness,.
3. The convection heat loss rate of CH_4/air flame is much higher than that of NH_3/air flame because of the higher gas temperature.

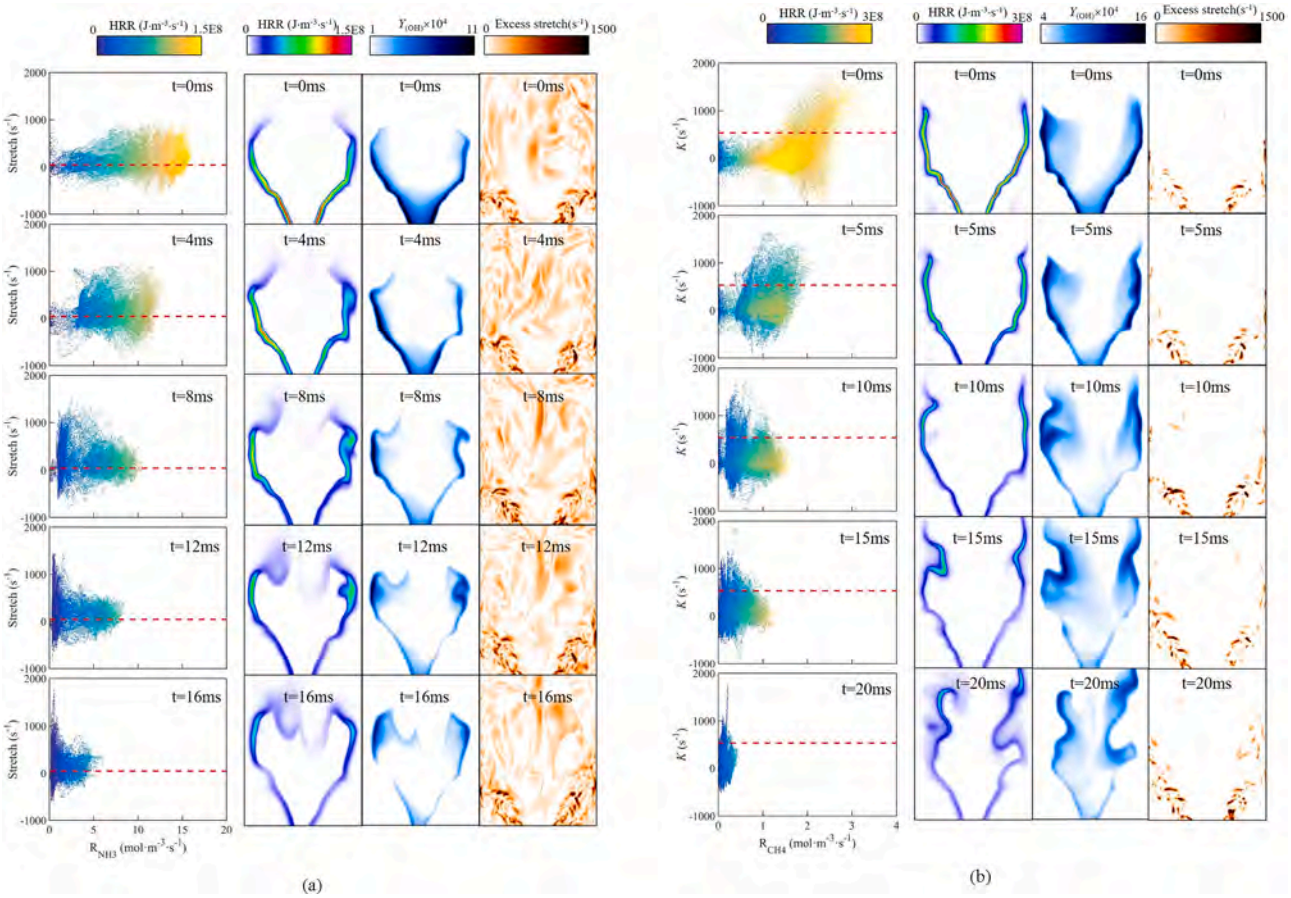

Fig. 12. Flame evolution by the joint PDF distributions of stretch rate and chemical reaction rate of fuel consumption R_{fuel}, evolutionary HRR, OH mass fraction as well as the excessive stretch extracted at different instances of (a) NH_3/air flame and (b) CH_4/air flame. The extinction stretch K_e is marked by red dotted lines. (For interpretation of the references to colour in this figure legend, the reader is referred to the web version of this article.)

However, the chamber wall heat loss shows greater influence on flame stabilization for NH_3/air flame, although the absolute value of convection heat loss rate of ammonia is less than that of methane.

4. Three different phases of the blow-off sequence can be defined, and a resistance of the heat release can be only observed in NH_3/air flames. In comparing, the blow-off of CH_4/air flame is mainly caused by the decreasing HRR and heat loss, while for NH_3/air flame, it is a combined effect of the excessive stretch, the reduction of HRR as well as the greater heat loss effect.

CRediT authorship contribution statement

Xutao Wei: Investigation, Formal analysis, Methodology, Writing - original draft. **Meng Zhang:** Methodology, Writing - review & editing, Formal analysis. **Zhenhua An:** . Methodology, Data curation, Writing - original draft. **Jinhua Wang:** Writing - review & editing, Supervision. **Zuohua Huang:** Writing - review & editing, Supervision, Funding acquisition. **Houzhang Tan:** Supervision.

Declaration of Competing Interest

The authors declare that they have no known competing financial interests or personal relationships that could have appeared to influence the work reported in this paper.

Acknowledgements

This work is supported by the Basic Science Center Program for Ordered Energy Conversion of the National Natural Science Foundation of China (No.51888103)

References

[1] Ikäheimo J, Kiviluoma J, Weiss R, Holttinen H. Power-to-ammonia in future North European 100 % renewable power and heat system. Int J Hydrogen Energy 2018; 43(36):17295–308.
[2] Valera-Medina A, Xiao H, Owen-Jones M, David WIF, Bowen PJ. Ammonia for power. Prog Energy Combust Sci 2018;69:63–102.
[3] Kobayashi H, Hayakawa A, Somarathne KDK, Okafor E. Science and technology of ammonia combustion. Proc Combust Inst 2019;37(1):109–33.
[4] Yang SJ, Jung H, Kim T, Park CR. Recent advances in hydrogen storage technologies based on nanoporous carbon materials. Progress in Natural Science: Materials International 2012;22(6):631–8.
[5] Valera-Medina A, Marsh R, Runyon J, Pugh D, Beasley P, Hughes T, et al. Ammonia–methane combustion in tangential swirl burners for gas turbine power generation. Appl Energy 2017;185:1362–71.
[6] Zamfirescu C, Dincer I. Using ammonia as a sustainable fuel. J Power Sources 2008; 185(1):459–65.
[7] Hayakawa A, Goto T, Mimoto R, Arakawa Y, Kudo T, Kobayashi H. Laminar burning velocity and Markstein length of ammonia/air premixed flames at various pressures. Fuel 2015;159:98–106.
[8] Hayakawa A, Arakawa Y, Mimoto R, Somarathne KDKA, Kudo T, Kobayashi H. Experimental investigation of stabilization and emission characteristics of ammonia/air premixed flames in a swirl combustor. Int J Hydrogen Energy 2017; 42(19):14010–8.
[9] Zhang M, Wei X, Wang J, Huang Z, Tan H. The blow-off and transient characteristics of co-firing ammonia/methane fuels in a swirl combustor. Proceedings of the Combustion Institute 2020. In press. doi: 10.1016/j.proci.2020.08.056.
[10] Syred N, Giles A, Lewis J, Abdulsada M, Valera Medina A, Marsh R, et al. Effect of inlet and outlet configurations on blow-off and flashback with premixed combustion for methane and a high hydrogen content fuel in a generic swirl burner. Appl Energy 2014;116:288–96.
[11] Xiao H, Valera-Medina A, Marsh R, Bowen PJ. Numerical study assessing various ammonia/methane reaction models for use under gas turbine conditions. Fuel 2017;196:344–51.

[12] Jójka J, Ślefarski R. Dimensionally reduced modeling of nitric oxide formation for premixed methane-air flames with ammonia content. Fuel 2018;217:98–105.
[13] Reiter AJ, Kong S-C. Combustion and emissions characteristics of compression-ignition engine using dual ammonia-diesel fuel. Fuel 2011;90(1):87–97.
[14] Gross CW, Kong S-C. Performance characteristics of a compression-ignition engine using direct-injection ammonia–DME mixtures. Fuel 2013;103:1069–79.
[15] Okafor EC, Naito Y, Colson S, Ichikawa A, Kudo T, Hayakawa A, et al. Measurement and modelling of the laminar burning velocity of methane-ammonia-air flames at high pressures using a reduced reaction mechanism. Combust Flame 2019;204:162–75.
[16] Henshaw PF, D'Andrea T, Mann KRC, Ting DSK. Premixed ammonia-methane-air combustion. Combust Sci Technol 2005;177(11):2151–70.
[17] Okafor EC, Yamashita H, Hayakawa A, Somarathne KDKA, Kudo T, Tsujimura T, et al. Flame stability and emissions characteristics of liquid ammonia spray co-fired with methane in a single stage swirl combustor. Fuel 2021;287:119433. https://doi.org/10.1016/j.fuel.2020.119433.
[18] Guo S, Wang J, Zhang W, Lin B, Wu Y, Yu S, et al. Investigation on bluff-body and swirl stabilized flames near lean blowoff with PIV/PLIF measurements and LES modelling. Appl Therm Eng 2019;160:114021. https://doi.org/10.1016/j.applthermaleng.2019.114021.
[19] Ma PC, Wu H, Labahn JW, Jaravel T, Ihme M. Analysis of transient blow-out dynamics in a swirl-stabilized combustor using large-eddy simulations. Proc Combust Inst 2019;37(4):5073–82.
[20] Guo S, Wang J, Zhang W, Zhang M, Huang Z. Effect of hydrogen enrichment on swirl/bluff-body lean premixed flame stabilization. Int J Hydrogen Energy 2020;45(18):10906–19.
[21] Somarathne KDKA, Hayakawa A, Kobayashi H. Numerical investigation on the combustion characteristics of turbulent premixed ammonia/air flames stabilized by a swirl burner. Journal of Fluid. Science and Technology 2016;11(4):JFST0026.
[22] Somarathne KDKA, Hatakeyama S, Hayakawa A, Kobayashi H. Numerical study of a low emission gas turbine like combustor for turbulent ammonia/air premixed swirl flames with a secondary air injection at high pressure. Int J Hydrogen Energy 2017;42(44):27388–99.
[23] Honzawa T, Kai R, Okada A, Valera-Medina A, Bowen PJ, Kurose R. Predictions of NO and CO emissions in ammonia/methane/air combustion by LES using a non-adiabatic flamelet generated manifold. Energy 2019;186:115771. https://doi.org/10.1016/j.energy.2019.07.101.
[24] Chong CT, Lam SS, Hochgreb S. Effect of mixture flow stratification on premixed flame structure and emissions under counter-rotating swirl burner configuration. Appl Therm Eng 2016;105:905–12.
[25] Zhang M, An Z, Wei X, Wang J, Huang Z, Tan H. Emission analysis of the CH4/NH3/air co-firing fuels in a model combustor. Fuel 2021;291:120135. https://doi.org/10.1016/j.fuel.2021.120135.
[26] Zhang W, Wang J, Lin W, Guo S, Zhang M, Li G, et al. Measurements on flame structure of bluff body and swirl stabilized premixed flames close to blow-off. Exp Therm Fluid Sci 2019;104:15–25.
[27] Lilly DK. A proposed modification of the Germano subgrid-scale closure method. Phys Fluids A 1992;4(3):633–5.
[28] Germano M, Piomelli U, Moin P, Cabot WH. A dynamic subgrid-scale eddy viscosity model. Phys Fluids A 1991;3(7):1760–5.
[29] Colin O, Ducros F, Veynante D, Poinsot T. A thickened flame model for large eddy simulations of turbulent premixed combustion. Phys Fluids 2000;12(7):1843–63.
[30] Charlette F, Meneveau C, Veynante D. A power-law flame wrinkling model for LES of premixed turbulent combustion Part II: dynamic formulation. Combust Flame 2002;131(1-2):181–97.
[31] Veynante D, Vervisch L. Turbulent combustion modeling. Prog Energy Combust Sci 2002;28(3):193–266.
[32] Wang G, Boileau M, Veynante D, Truffin K. Large eddy simulation of a growing turbulent premixed flame kernel using a dynamic flame surface density model. Combust Flame 2012;159(8):2742–54.
[33] Guo S, Wang J, Wei X, Yu S, Zhang M, Huang Z. Numerical simulation of premixed combustion using the modified dynamic thickened flame model coupled with multi-step reaction mechanism. Fuel 2018;233:346–53.
[34] Durand L, Polifke W. Implementation of the Thickened Flame Model for Large Eddy Simulation of Turbulent Premixed Combustion in a Commercial Solver. ASME Turbo Expo 2007: Power for Land, Sea, and Air 2007;2:869-78.
[35] Tian Z, Zhang L, Li Y, Yuan T, Qi F. An experimental and kinetic modeling study of a premixed nitromethane flame at low pressure. Proc Combust Inst 2009;32(1):311–8.
[36] Konnov AA. Implementation of the NCN pathway of prompt-NO formation in the detailed reaction mechanism. Combust Flame 2009;156(11):2093–105.
[37] Miller J, Smooke M, Green R, Kee R. Kinetic-Modeling the Oxidation of Ammonia in Flames. Combust Sci Technol 1983;34:149–76.
[38] Stagni A, Cavallotti C, Arunthanayothin S, Song Yu, Herbinet O, Battin-Leclerc F, et al. An experimental, theoretical and kinetic-modeling study of the gas-phase oxidation of ammonia. React Chem Eng 2020;5(4):696–711.
[39] Mathieu O, Petersen EL. Experimental and modeling study on the high-temperature oxidation of Ammonia and related NOx chemistry. Combust Flame 2015;162(3):554–70.
[40] Otomo J, Koshi M, Mitsumori T, Iwasaki H, Yamada K. Chemical kinetic modeling of ammonia oxidation with improved reaction mechanism for ammonia/air and ammonia/hydrogen/air combustion. Int J Hydrogen Energy 2018;43(5):3004–14.
[41] Chen J, Jiang X, Qin X, Huang Z. Effect of hydrogen blending on the high temperature auto-ignition of ammonia at elevated pressure. Fuel 2021;287:119563. https://doi.org/10.1016/j.fuel.2020.119563.
[42] Xiao H, Howard M, Valera-Medina A, Dooley S, Bowen PJ. Study on Reduced Chemical Mechanisms of Ammonia/Methane Combustion under Gas Turbine Conditions. Energy Fuels 2016;30(10):8701–10.
[43] CHEMKIN-PRO 17.2. ANSYS, Inc: San Diego.
[44] Lieuwen T, Murray N. Unsteady combustor physics. J Acoustical Soc Am 2013;134:1431.
[45] Somarathne KDKA, Okafor E C, Hayakawa A, Kudo T, Kurata O, Iki N, et al. Emission characteristics of turbulent non-premixed ammonia/air and methane/air swirl flames through a rich-lean combustor under various wall thermal boundary conditions at high pressure. Combust Flame 2019;210:247–61.
[46] Bilger RW. The structure of turbulent nonpremixed flames. Symp (Int) Combust 1989;22(1):475–88.
[47] Kuenne G, Seffrin F, Fuest F, Stahler T, Ketelheun A, Geyer D, et al. Experimental and numerical analysis of a lean premixed stratified burner using 1D Raman/Rayleigh scattering and large eddy simulation. Combust Flame 2012;159(8):2669–89.
[48] Pires Da Cruz A, Dean AM, Grenda JM. A numerical study of the laminar flame speed of stratified methane/air flames. Proceedings of the Combustion Institute 2000;28(2):1925-32.
[49] Holman JP. Heat transfer. 10th ed. New York: McGraw-Hill; 2010.